Intermediate-depth icequakes and harmonic tremor in an Alpine glacier (glacier d 'Argentiere,France): evidence for hydraulic fracturing

Agnes Helmstetter, Luc Moreau, Barbara Nicolas, Pierre Comon, Michel Gay

Intermediate-depth icequakes and harmonic tremor in an Alpine glacier (Glacier d'Argentière, France) : evidence for hydraulic fracturing?

Agnès Helmstetter[1], Luc Moreau[2], Barbara Nicolas[3], Pierre Comon[3] and Michel Gay[3]
[1] Univ. Grenoble, ISTerre, CNRS, Grenoble, France.
[2] EDYTEM, CNRS, Chambéry, France.
[3] Grenoble INP, GIPSA-Lab, CNRS, Grenoble, France.

Abstract

We detected several thousand deep englacial icequakes on Glacier d'Argentière (Mont-Blanc Massif) between 30 March and 3 May 2012. These events have been classified in eight clusters. Inside each cluster, the waveforms are similar for P-waves and S-waves, although the time delay between the P-waves and S-waves vary by up to 0.03 s, indicating an extended source area. Although these events were recorded by a single accelerometer, they were roughly located using a polarization analysis. The deepest events were located at a depth of 130 m, 60 m above the ice/bed interface. The clusters are separated in space. The largest cluster extends over about 100 m. For this cluster, the strike of the rupture plane is nearly parallel to the direction of the open crevasses, and the dip angle is 56 degrees. Deep icequakes occur in bursts of activity that last for a few hours and are separated by quiet periods. Many events occurred on 28 and 29 April 2012, during the warmest days, when snowmelting was likely important. The distributions of interevent times and peak amplitudes obey power laws, as also observed for earthquakes, but with larger exponents. The polarity of the P-waves for all of the events is consistent with tensile faulting. Finally, between 25 April and 3 May, we observed a gliding harmonic tremor with a fundamental resonance frequency that varied between 30 Hz and 38 Hz, with additional higher frequency harmonics. During this time we also observed shallow hybrid events with high-frequency onsets and a monochromatic coda. These events might be produced by the propagation of fractures and the subsequent flow of water into the fracture. The strongest resonance was observed just after a strong burst of deep icequakes, and during an unusually warm period when the snow height decreased by 60 cm in one week. The resonance frequency shows a succession of several sharp decreases and phases of progressive increases. One of the strongest negative steps of the resonance frequency on 28 April coincides with a burst of deep icequakes. These events appear to be associated with the propagation of fractures, which can explain the decrease in the resonance frequency. Finally, we observed an acceleration of glacier flow on 29 April, suggesting that meltwater had reached the ice/bed interface. These observations suggest that deep icequakes are due to hydraulic fracturing, and that they can be used to track fluid flow inside glaciers.

1 Introduction

Alpine glaciers produce a wide variety of seismic signals. The most frequent seismic events are shallow icequakes that are associated with fracture opening or propagation [*Neave and Savage*(1970), *Mikesell, et al.*(2012)] and to the collapse of large ice blocks [*O'Neel et al.*(2007), *Roux et al.*(2008)]. Basal icequakes are much less frequent. These can be produced by the opening or closing of tensile faults near the ice/bed interface due to changes in the basal water pressure [*Walter et al.*(2010), *Walter et al.*(2013)], or by basal slip [*Helmstetter et al.*(2014)]. Seismic events have also been detected at intermediate depths that are below the usual depth of open crevasses, but are above the ice/bed interface [*Deichmann et al.*(2000), *Walter et al.*(2008), *Walter et al.*(2009), *Röösli et al.*(2014)]. These events might be due to hydraulic fracturing. Given sufficient water supply, a water-filled fracture can propagate to the base of a glacier when the overburden stress at the fracture tip is offset by the density contrast between the ice and water [*Van der Veen*(1998), *Van der Veen*(2007), *Carmichael et al.*(2012)]. Under certain circumstances, bottom crevasses might also propagate upward [*Van der Veen*(1998)].

Finally, another class of seismic signals detected on glaciers is produced by the resonance in subglacial water-filled cracks and conduits. This class includes low-frequency events [*St. Lawrence and Qamar*(1979), *Métaxian, et al.*(2003)], hybrid events [*West et al.*(2010)], and tremors [*Winberry et al.*(2009), *Heeszel et al.*(2014), *Röösli et al.*(2014)]. Hybrid events are characterized by high-frequency onset followed by lower-frequency coda, similar to signals detected on volcanoes [*West et al.*(2010), *Röösli et al.*(2014)]. They are interpreted as due to the opening of englacial fractures and the subsequent flow of water into the fractures. Subglacial water flow can also produce harmonic seismic tremors that can last for several hours [*Röösli et al.*(2014), *Heeszel et al.*(2014)]. However, harmonic tremor can also be produced by the repeated failure of small subglacial asperities [*Winberry et al.*(2013)].

In this report, we have studied intermediate-depth icequakes detected at Glacier d'Argentière (Mont-Blanc massif) in the spring of 2012. Most seismic signals are likely associated with shallow sources, as either serac falls or crevassing [*Neave and Savage*(1970), *Deichmann et al.*(2000), *Roux et al.*(2008), *Walter et al.*(2008)]. We have also identified two classes of deep icequakes that are characterized by higher frequencies, shorter durations, and distinct P-waves and S-waves. In the first part of this two-part submission [*Helmstetter et al.*(2014)], we have analyzed the first class of deep events, and we suggest that these events were associated with repeated ruptures of asperities that were located at the ice/bed interface. Here, we focus on the second class of deep events, which are located at intermediate depths that are deeper than the depth of open crevasses (about 20 m) but are above the bedrock. We describe the distribution of these events in time, space and magnitude, and discuss the possible mechanisms that are responsible for these events. We also analyze the spectral content of the seismic noise, which shows a resonance at a frequency of about 35 Hz. Several methods used in this study (e.g., detection and location of seismic sources) were also used for the analysis of the basal icequakes. More details on these methods are given in [*Helmstetter et al.*(2014)].

2 Study area and instrumentation

Glacier d'Argentière is a temperate glacier in the Mont Blanc massif in the French Alps. This glacier has a length of about 10 km, from its top part at an altitude of 3400 m a.s.l., to its tongue at an altitude of 1600 m a.s.l.. We installed an accelerometer in the ablation zone, at an elevation of 2380 m, about

600 m upstream from Lognan icefall. At this location, the glacier moves on average by 18 cm per day, and the maximum ice thickness is approximately 200 m [*Vincent et al.*(2009)]. Figure 1 shows an aerial photograph of the glacier, with the location of the accelerometer. The seismometer was in operation during five time windows that covered 44 days between February and June 2012: 17-25 February, 12-17 March, 30 March to 12 April, 25 April to 3 May, and 5-19 June. The gaps in the monitoring were due to difficult glacier access, insufficient power supply and limited data storage capacity. The accelerometer was a MEMS-based Sercel DSU3 that recorded in continuous mode at a sampling rate of 1000 Hz. Due to the high frequency content of the deep icequake signals, the data was undersampled. In future studies, the sampling rate should be increased to 2000 Hz, to avoid potential aliasing effects and to improve location accuracy. The sensor was installed in winter by digging 2 meters into the snow layer down to the snow/ice interface. On 9 May, there was still 2.5 m of snow above the sensor. Therefore, we are confident that the orientation of the sensor remained correct throughout the time interval of 30 March to 3 May that was analyzed in this study.

A permanent meteorological station is installed near the seismic sensor (Figure 1, circle). This station provides temperature, but has no measure of precipitation. The meteorological data are available from the GLACIOCLIM database [*Vincent et al.*(2009)]. We also used data from two stations from Météo-France. One of these stations is installed 4 km north of the network (Le Tour village) at an elevation of 1500 m a.s.l., and this was used to obtain the precipitation data. The other station is located in the Aiguilles Rouges massif, at approximately the same elevation (2365 m a.s.l.) as our network and at about 7 km to the west; this station provided the snow height measurements.

Under Glacier d'Argentière, the water-collection tunnels constructed by Emosson S.A. allow access to several natural and permanent subglacial cavities beneath the Lognan ice fall, at an elevation of 2180 m a.s.l. The glacier basal sliding velocity has been measured since 1970 in one of these cavities, using a cavitometer [*Vivian and Bocquet*(1973), *Bocquet and Ricq*(1977), *Moreau*(1999)]. This instrument is made of a wheel that is kept in contact with the ice by a spring that acts on an articulated arm.

3 Detection and classification

We applied an automatic detection method based on the spectrogram of the seismic signal to obtain a catalog of seismic events [*Helmstetter and Garambois*(2010)]. This method provides a list of events with their characteristics (e.g., peak amplitude, duration, dominant frequency). We then looked manually at all of the events to classify them as shallow icequakes, serac fall, or deep icequakes. Examples of waveforms for these different types of events are shown in Figure 2. The signals in this Figure 2 were converted into ground velocity to allow for comparisons with signals presented in previous studies. Unlike shallow icequakes, the deep events are characterized by very short durations (< 0.1 s), an impulsive onset, distinct P-waves and S-waves, and the absence of surface waves [*Deichmann et al.*(2000), *Walter et al.*(2008)]. The deep events were further classified as either basal or intermediate-depth icequakes, based on the source depth. The basal events were analyzed in [*Helmstetter et al.*(2014)], while the present study focuses on the intermediate-depth events. These intermediate-depth events were located at least 60 m above the ice/bed interface, but generally below the surface crevassing zone. These events are referred to as "deep icequakes" in the following.

By looking at the seismograms of these deep icequakes, they could be classified into several clusters, with very similar waveforms within each cluster. The time delay between the P-waves and S-waves varies by up to 0.03 s within one cluster, corresponding to a change in the source-sensor distance of

87 m. To detect events that belonged to each cluster, we performed cross-correlation of a template event with the full continuous database. The template event was first chosen randomly by picking one event in our list of deep events. As the time delay between the P-waves and S-waves varies significantly within each cluster, we separately cross-correlated the signals for the P-waves and S-waves and allowed for a variation of 50% in the time delay between the P-waves and S-waves relative to the template event. We fixed a minimum correlation of 0.6 to classify signals into clusters. We then inspected visually all of the signals, and rejected those events that were significantly different by eye from the template event. We sometimes found waveforms that were different from the template, but were nonetheless typical of deep icequakes. In this case, these waveforms were associated with a new cluster, and were used as new template events. When an event was detected by several templates, we chose the template with the highest correlation. We then updated the template signal by stacking all of the events in each cluster. Before stacking the signals, we aligned the signals in time, and normalized each signal according to its peak amplitude. We cut each signal into two parts between the P-wave and S-wave arrival times. Each part of the signal for the P-waves and S-waves was aligned separately, by cross-correlation with the template signal.

We identified eight clusters of deep icequakes, which are labeled as A-H, and these contained between 220 and 5578 events. The waveforms of the template event of each cluster are shown in Figure 3. For each cluster and each component, the gray shaded areas in Figure 3 represent the standard deviations of the signals for all of events in the cluster (after normalization and alignment). All of the signals show impulsive P-waves and S-waves that were separated by a few hundredths of a second. The polarity and the relative amplitude of the P-waves and S-waves for the three components vary from one type of events to another. Types A and B differ only by the presence of multiple P-wave arrivals for the second type, while the waveforms for cluster A are simpler. Similarly, the waveforms for clusters C and G are similar to clusters D and H, respectively, but the signals for clusters C and G are simpler. The events of clusters B, D and H occurred about one month later than those for clusters A, C and G. For all types of events, the polarity of the P-wave arrival on the vertical component is upward. This is compatible with tensile failure, as suggested by [*Walter et al.*(2009)] from a moment tensor inversion of deep icequakes on Gornergletscher.

Most of the events that were identified occurred between 30 March and 3 May, 2012, with only nine deep icequakes detected earlier. We thus focused on this period in this study. Note that we might have missed events of different types. We did not look systematically at all of the events. We only identified eight different types of deep icequakes, and we searched for similar events in the full continuous database by cross-correlation with a template.

4 Location of seismic sources

We can roughly locate the source of these icequakes even with a single sensor. First, the distance between the source and the sensor can be estimated from the time delay between the P-waves and the S-waves

$$d = \frac{t_S - t_P}{1/V_S - 1/V_P} \ , \tag{1}$$

where t_P and t_S are the arrival times of the P-waves and S-waves, respectively. We assumed a uniform seismic-wave velocity of 3600 m/s for the P-waves, and 1610 m/s for the S-waves. These values were measured by [*Vallon*(1967)] for Glacier du Tacul, which is a temperate glacier in the Mont Blanc massif that is at about the same altitude as our seismometer. To estimate more precisely the time delay $t_S - t_P$

between the P-waves and S-waves, we fit each signal of a given cluster using the following signal, as in [*Helmstetter et al.*(2014)]:

$$y_t(t) = y_{t,P}(t - \Delta t_P) + y_{t,S}(t - \Delta t_S) \tag{2}$$

where $y_{t,p}$ and $y_{t,s}$ are the parts of the template event that correspond to the P-waves and S-waves, respectively, and Δt_P and Δt_S are the time delays, respectively. For each signal, we searched for the values of Δt_P and Δt_S that maximize the correlation between this signal and the template event y_t. The inversion started with a grid search with maximum time shifts of 1 ms for the P-waves and 20 ms for the S-waves. Then the best values of Δt_P and Δt_S were chosen as the starting values of a simplex optimization [*Nelder and Mead*(1965)]. We obtained a relative accuracy for the time delays on the order of 0.1 ms, about one tenth of the sampling rate. However, the absolute accuracy was much larger, as it was on the order of 1 ms. In addition, the direction of the source can be estimated by analysis of the polarization of the particle motion [*Vidale*(1986)]. We selected the time window associated with the P-waves, from the picked arrival time t_P to $t_P + 0.006$ s. We then applied a singular value decomposition to the analytic signal, without integration or filtering. The azimuth α of the source and the apparent angle of incidence ϕ were estimated from the direction of the first eigenvector. The apparent angle of incidence of the P-waves is, however, different from the direction of propagation, because it is affected by reflections at the free surface. We thus used the method of [*Neuberg and Pointer*(2000)] to correct for this effect. Assuming a planar free surface, the true angle of incidence ϕ_c can be estimated from the apparent angle ϕ by:

$$\phi_c = \sin^{-1}\left(\frac{V_P}{V_S}\sin\frac{\phi}{2}\right) \ . \tag{3}$$

Before applying this correction, we subtracted the surface slope along direction α from the apparent incidence angle. The surface slope around the seismometer reached 8 degrees along the glacier flow direction. Equation (3) has no real solution for $\phi > \phi^*$ with $\phi^* = 2\sin^{-1}\left(\frac{V_S}{V_P}\right) = 53$ degrees. The source depth z is given by $z = d\cos(\phi_c)$ and it varied between 0 and about 130 m. For incidence angles $\phi \approx \phi^*$, small errors on ϕ yield large uncertainties on ϕ_c, and therefore on the depth. We found 13% of events with an estimated incidence angle $\phi > \phi^*$, which should not be observed due to free surface effects. For these events, we could not estimate ϕ_c nor the source depth. Values of $\phi > \phi^*$ might be due to uncertainties in the estimated apparent incidence angle or to diffracted waves on the fractures. An example of waveforms and particle motion is shown in Figure 4. The polarization of the P-waves and S-waves is not perfectly linear, as would be expected for body waves. This might indicate heterogeneity, surface effects, or the influence of reflected waves at the ice/bed interface.

The polarization analysis and the correction (3) were validated with numerical simulations, earthquakes with known location, and basal icequakes detected by two 3-component stations [*Helmstetter et al.*(2014)]. In this study, we performed additional tests on synthetic seismograms to determine the influence of undersampling. We generated 1000 synthetic seismograms with uniform distributions of source depth between 20 m and 150 m, epicentral distances between 0 m and 100 m, assuming tensile faulting on planes with dip between 0 and 90 degrees, and strike between 0 degrees and 360 degrees. We assumed a point source with a rise time of 1 ms (i.e., duration of displacement) and an attenuation factor $Q = 20$ for both P-waves and S-waves [*Helmstetter et al.*(2014)]. We computed the ground acceleration with a sample rate of 3000 Hz, and then undersampled the signal down to 1000 Hz. We applied the same polarization analysis as for the real signals of deep icequakes, using a sample length of 6 ms. We also assumed a standard error of 1 ms on t_P and t_P. We obtained a

standard error of 12 degrees for the azimuth and 2 degrees for the incidence angle. The median absolute errors are much smaller, because the error distributions are not Gaussian, with median errors of 0.4 degrees for the azimuth and 0.2 degrees for the incidence angle. Surprisingly, the vertical location error (standard error, 3.2 m) is smaller than the horizontal error (standard error, 4.3 m). The vertical location error is larger for the shallowest events, because the incidence angle is close to ϕ^*, and small variations of the incidence angle when $\phi \approx \phi^*$ yield large variations of the corrected incidence angle ϕ_c estimated from Equation (3).

The location uncertainty is, however, much larger for real signals, and is difficult to evaluate due to poor signal-to-noise ratio, coarse sample rate, and heterogeneity of the seismic wave velocities. One way to evaluate the accuracy of the location is to analyze the distance between successive events. Events that occur very close in time are likely to also be very close in space. We selected all of the events with an amplitude $A > 200\ \mu m/s^2$ and a correlation with the template $C > 0.7$. For each event, we measured the distance between this event and the next event of the same cluster, and obtained a median distance of 15 m. However, this method overestimates the location accuracy, because successive events are likely in a similar location, with a similar source mechanism and source-receiver path. [*Helmstetter et al.*(2014)] applied the same location method to basal icequakes, and found good agreement between the icequake depths and the glacier thickness, with a mean difference of 2 m and a standard error of 18 m. This further suggests that the location accuracy (one standard error) is on the order of 18 m, although the depth of the shallow events is more uncertain when $\phi \approx \phi^*$.

A map of the icequakes is shown in Figure 5, for all of the events with $A > 300\ \mu m/s^2$, $C \geq 0.7$ and $\phi < \phi^*$. Each cluster has a distinct location and extends over several tens of meters. Most events are deeper than the maximum depth of open crevasses (about 20 m below the surface [*Paterson*(1994)]), but shallower than the ice/bed interface. Clusters A, C and G, which occurred before 13 April, were much shallower than the other clusters that were only active after 25 April. The average depth was 30 m before 25 April, and 70 m after this date. The deepest events at ≈ 130 m occurred in the central part of the glacier, where the ice thickness was approximately ≈ 190 m [*Vincent et al.*(2009)]. This implies that the fractures that generated these icequakes did not reach the glacier bottom, or that the fracture propagation below 130 m depth was aseismic.

The depth of the icequakes for cluster B varied with time. Figure 6 shows a complex pattern with successive increases and decreases in the source depth with time. Before 25 April, the depth of the icequakes ranged between 20 m and 50 m, with a mean of 30 m. When the temperature rose after 25 April, up to 9 degrees C (Figure 7c), the average depth increased up to 70 m, and the maximum icequake depth reached 130 m. In the morning of 28 April, the depth increased gradually from 60 m to 85 m in 1.4 hour, at a mean rate of 18 m/hr. During the last days of the acquisition after 30 April, the temperature decreased below freezing and the mean icequake depth decreased. These observations suggest that higher temperatures increased meltwater production, which raised the water level in fractures and promoted propagation of the fractures at depth.

There is likely a smooth transition between the shallow and deep seismic activities. For the shallowest events detected, the P-waves and S-waves overlapped. Therefore, closer events cannot be detected in the first step of our detection procedure, when separately correlating the continuous signal with the P-waves and S-waves of the template signal.

To analyze the spatial structure of the largest cluster, B, we used principal component analysis of the three-dimensional cloud of points [*Michelini and Bolt*(1986)]. We estimated the plane that best matched cluster B from the first two eigenvectors. We then computed the strike direction and the dip angle of this plane. We found a strike of 67 degrees, which is nearly parallel to the direction of the open crevasses near this cluster, a dip angle of 56 degrees, and a planarity coefficient of 0.7. This coefficient

is defined by $1 - 2\lambda_3/(\lambda_1 + \lambda 2)$, where $\lambda_1 > \lambda_2 > \lambda_3$ are the three eigenvalues, and it ranges between 0 (no structure in space) and 1 (all points belong to the same plane).

The polarity of the P-waves for all of the clusters and all of the components are consistent with tensile failure (positive in the direction away from the source), as also observed by [*Carmichael et al.*(2012)]. On the other hand, shear failures produce mixed first-motion polarities. A single-station and single-source polarity measurements thus cannot exclude shear sources. However, as all of the eight clusters with different source azimuths have compressive P-wave polarities, this argues against a shear source mechanism.

The orientation of the fractures at depth can also be observed from boreholes. [*Vallon*(1981)] drilled a borehole into Glacier d'Argentière in 1980, at an elevation close to our network (a few hundred meters above Lognan ice fall), but closer to the side, at about 200 m from the right side of the glacier. He observed two families of fracture planes with a dip angle that decreased with depth, from about 80 degrees at 40 m down to about 0 degrees at the ice/bed interface at a depth of 240 m. The first family of fractures corresponded at the surface to marginal crevasses with an angle of about 45 degrees from the margin. These fractures had a right-lateral motion that was consistent with the glacier motion being slower near the sides than at the center of the glacier. [*Fountain et al.*(2005)] also observed fractures at depth in boreholes for a small Swedish glacier. They suggested that steeply dipping fractures with openings on the order of several centimeters provide the main pathways of water flow in temperate glaciers. These features can be observed from near the surface down to a few meters above the glacier bottom. Their strikes are generally parallel to the direction of the surface crevasses.

5 Distribution of events in time and size

Figure 7 illustrates the temporal variations of the seismic activity, meteorological parameters, snow height, and basal displacement. The seismic activity was very intermittent, with quiet periods that were separated by bursts of activity with several hundreds of events per hour. Each burst usually involved only one cluster, and lasted for a few hours. In contrast, the rate of shallow icequakes (Figure 7b, gray line) was much less sporadic than deep events. Shallow icequakes were more frequent after 27 April, although the fluctuations of the rate of shallow events were not clearly related to the rate of deep events. During bursts of deep icequakes, there were more deep events than shallow ones. However, when looking at the whole duration of the study, there were many more shallow events than deep icequakes.

During the first acquisition period, which was between 30 March and 12 April, the temperature was beneath freezing most of the time (Figure 7c), so that meltwater production was very small. The highest peak of activity occurred on 4 April at noon (14:00 local time), with 507 events in one hour. Before 12 April, there is no apparent correlation between the icequakes and the precipitation. Strong precipitation occurred between 21 and 25 April, with a total of 40 mm of water that yielded 57 cm of snow at the meteorological station of Aiguilles Rouges (elevation of 2365 m, about 7 km to the west of the study area). Then between 25 and 27 April, the mean daily temperatures rose from -7 degrees C up to 9 degrees C. During this warming episode, the snow height decreased by 60 cm (snowmelt and/or compaction). This strong increase in the temperature was followed on 28 April by a strong peak of the rate of deep icequakes, and by acceleration of the glacier flow. During the following days, both the temperature and the rate of deep icequakes decreased on average. Two small bursts of deep icequakes on the evenings of 30 April and 1 May coincided with precipitation.

[*Carmichael et al.*(2012)] detected icequakes at Taylor Glacier, Antarctica, which were clearly asso-

ciated with episodes of surface melt. Surface melt events produced an increase in the background rate of icequakes. These icequakes were located near surface cracks, but their depths were not constrained. The slow variation of icequake activity observed in this study is more similar to our observation of the rate of shallow icequakes than with intermittent deep icequakes.

The rate of deep icequakes shows only weak daily fluctuations (Figure 8). There is a strong peak of activity around 14:00 local time, although this is due to a single burst of activity on 4 April. This peak disappears when removing the events for this day, although there are still slightly more events during the day than at night. The daily distribution does not change when the minimum amplitude of the events is increased from 300 $\mu m/s^2$ up to 1000 $\mu m/s^2$, which suggests that it is not affected by daily changes in noise level and completeness threshold.

To characterize the temporal clustering of the deep events, we estimated the probability density function of the interevent times, as shown in figure 9a. For events with peak amplitude $A > 100$ $\mu m/s^2$, this distribution was fitted by a power-law of exponent 1.66 for the interevent times longer than 10 s. When increasing the amplitude threshold to $A > 1000$ $\mu m/s^2$, we found an exponent 1.48 for the interevent times longer than 50 s. The cut-off for times shorter than 0.1 s is likely a detection bias, as events separated by a time shorter than the signal duration are difficult to separate. The roll-off for times longer than 10^5 s (about one day) is due to the limited duration of our catalog. In the time interval of 0.1 s to 10 s, there is an intermediate power-law regime with a smaller exponent, of ≈ 0.3. This change of exponent for the interevent times of about 10 s is likely real and not due to a detection problem, because this time is much longer than the signal duration and because this crossover occurs at a longer time ≈ 50 s for the largest events with $A > 1000$ $\mu m/s^2$. This distribution of interevent times is similar to that obtained for earthquakes, but with an exponent 1.6 larger than the value ≈ 1 that is commonly reported for earthquakes [*Bak et al.*(2002)]. For earthquakes, the power-law distribution of the interevent times was explained by earthquake interactions. Each earthquake can trigger aftershocks with a rate that decays as a power law of time since the triggering event, and increases exponentially with the magnitude of the triggering event [*Helmstetter et al.*(2005)]. However, this model does not explain the temporal clustering of deep icequakes. We have estimated the average rate of deep icequakes as a function of the time since a deep icequake and of the amplitude of this icequake, as was done for earthquakes in [*Helmstetter et al.*(2005)]. Unlike for earthquakes, we found that the average rate of activity after an event does not depend on its amplitude. Clustering in time might therefore arise from short-term fluctuations of an external forcing mechanism, which might be water pressure, rather than interactions between events.

The deep icequakes show a wide range of peak amplitudes, ranging from 97 $\mu m/s^2$ up to 13950 $\mu m/s^2$. After the integration of the signals, the peak ground velocity ranged between 62 nm/s and 11474 nm/s. The distribution of the peak amplitude is shown in Figure 9. This can be fitted by a power law with an exponent of 3.5 for amplitudes between 1000 $\mu m/s^2$ and 10000 $\mu m/s^2$. Previous studies also found a power-law distribution of icequake amplitudes, but with a smaller exponent ≈ 1 [*Roux et al.*(2008), *Faillettaz et al.*(2011), *Dalban Canassy et al.*(2013)]. These data sets were likely dominated by shallow events, which might have a different magnitude distribution. As in the time domain, the distribution of the peak amplitudes for icequakes is similar to that observed for earthquakes, although the exponent is much larger for icequakes than earthquakes [*Bak et al.*(2002)]. [*Weiss*(1997)] showed that a power law distribution of peak amplitudes corresponds to an exponential distribution of magnitudes (i.e., the Gutenberg-Richter law) with the same exponent b, even if the amplitudes are not corrected for attenuation with distance (geometric and anelastic attenuation). For earthquakes, the exponent b of the Gutenberg Richter law is larger for induced earthquakes than for tectonic events [*Grünthal*(2013)]. For geothermal projects, where earthquakes are induced by hydraulic fracturing,

the b value is 1.94, compared with $b = 1.16$ for tectonic earthquakes. The large b value found for our database of deep icequakes might thus be related to the triggering mechanism, which is suspected to be hydraulic fracturing. However, the failure mechanism is different for induced earthquakes (i.e., mostly shear failure) and for deep icequakes (i.e., tensile failure), and the b value might depend on the failure mechanism. Indeed, [*Schorlemmer et al.*(1997)] suggested that the b value for earthquakes varies systematically for different styles of faulting, with higher b values corresponding to lower stress.

6 Seismic noise and resonance frequency

We observed a resonance of the seismic signal during part of our acquisition. This resonance was seen both in the seismic noise and in the coda of shallow and deep icequakes. An example of a hybrid icequake, with high-frequency onset followed by lower frequency monochromatic coda is shown in Figure 10. Between 25 April and 3 May, 45% of the shallow events had a peak frequency between 30 Hz and 40 Hz, compared with only 14% before 13 April. Similar hybrid events were detected by [*West et al.*(2010)] in Alaska. These events were interpreted as brittle fractures that were driven by fluids, or hydraulic fracturing, followed by resonances caused by the rush of water into the newly opened space. The spectrogram of the continuous seismic signal is shown in Figure 11a for the time interval of 30 March to 3 May. The signal was first clipped at a maximum amplitude of 100 $\mu\ m/s^2$, to weaken the influence of seismic events. We computed the power spectrum of the vertical component of the signal for nonoverlapping time windows of 1 min. We then took the geometric average over 10 successive windows. During the first acquisition period, between 30 March and 12 April, there is no apparent resonance. Resonance at a frequency of about 35 Hz appeared during the gap between 12 and 25 April, and lasted until the end of the second acquisition on 3 May 2012. The resonance frequency f_r is shown in Figure 11b. For each time window of 10 min, we normalized the power spectrum by the average spectrum, and we computed the maximum value of the normalized spectrum in the frequency range of 20 Hz to 50 Hz. The maximum value of the normalized spectrum is defined as the amplification and this is shown in Figure 11b. The main resonance frequency varied with time between 30 Hz and 38 Hz. Several other weaker resonances are also visible at higher frequencies, and these show the same temporal variations as the dominant frequency. The resonance at about 250 Hz on 28 and 29 April is also visible in the seismograms of deep icequakes that occurred during this time period. Figure 3 shows that clusters B, D, E, F and H, which were active during the harmonic tremor, had longer coda for the P-waves, with a frequency of about 250 Hz. In contrast, clusters A, C and G were only detected before 12 April, and had much simpler waveforms.

A quick drop in f_r from 33 Hz down to 30 Hz occurred on 28 April at 14:00 UTC (16:00 local time), during the largest burst of the deep icequakes. The amplification increased up to a factor of 20 until midnight on 28 April, and then it decreased. A first peak of amplification was observed on 27 April, and this coincided with a small burst of deep and shallow icequakes. The strongest resonance occurred during a relatively quiet period that followed the main burst of deep icequakes. After this time, the resonance frequency and the amplification fluctuated, and the rate of shallow and deep icequakes remained higher than before 25 April. However, there was no obvious link between the resonance frequency and amplification and the rate of deep icequakes after 29 April.

Other studies have also observed seismic resonance due to fluid flow inside glaciers [*St. Lawrence and Qamar*(1979), *Métaxian, et al.*(2003), *West et al.*(2010), *Heeszel et al.*(2014), *Röösli et al.*(2014)]. [*St. Lawrence and Qamar*(1979)] attributed the seismic source of monochromatic low-frequency icequakes to hydraulic transients that were generated by abrupt changes in water flow

through subglacial conduits. Another mechanism for harmonic or hybrid signals is the resonance of fluid-filled cavities [*Chouet*(1986), *Métaxian, et al.*(2003), *Winberry et al.*(2009), *Heeszel et al.*(2014)]. Assuming Stoneley guided waves in a fluid-filled fracture, the resonance frequency decreases with increasing crack length and increases with crack thickness [*Korneev*(2008), *Tary et al.*(2014)]. A resonance frequency of 20 Hz can be explained by a crack length of 5 m and a thickness of 2 cm [*Heeszel et al.*(2014)]. However, the resonance frequency alone cannot constrain the fracture geometry, because there is a trade-off between fracture width and fracture length. Observed temporal changes in f_r might thus be explained by the propagation of fractures or by their progressive opening or closing. It is important to note that the relevant length that controls the resonance frequency in this model is not the full length of the fracture, but only the part that is filled with water. In our case, there are likely important temporal variations of the water level inside the fractures if they are connected with the surface. Therefore, our observed changes in the resonance frequency probably highlight temporal changes in the water level, rather than changes in the length or width of fractures. Similar observations were reported by [*Röösli et al.*(2014)], who observed harmonic tremor induced by a moulin, with temporal fluctuations of the resonance frequency correlated with temporal fluctuations of the water level measured inside the moulin.

Finally, gliding harmonic tremor can also be produced by the repeated failure of small subglacial asperities. [*Winberry et al.*(2013)] recorded repeating basal icequakes and a gliding harmonic tremor during the rupture propagation of a glacial earthquake underneath Whillans Ice Stream in Antarctica. The emergent tremor was composed of discrete slip events, although these events were not clearly discernible. The temporal variation of the frequency was correlated with the surface speed of the ice stream. We do not think that this mechanism can explain our observations, as in our case the resonance was also visible in the coda of the shallow icequakes (Figure 10).

Our results are similar to the study of [*Heeszel et al.*(2014)], who observed a gliding harmonic tremor and high frequency deep basal icequakes during a glacier lake outburst at Gornergletscher. The harmonic tremor had a slowly decaying resonance frequency of about 20 Hz with several higher frequency harmonics and several sudden step changes. The resonance frequency of deep icequakes progressively varied between 100 Hz and 200 Hz. The P-wave polarity for these events suggests that they were due to crack closing. [*Heeszel et al.*(2014)] interpreted the increase in the resonance frequency with time as due to closing fractures. Similar observations of gliding harmonic tremor have also been observed for volcanoes [*Konstantinou and Schlindwein*(2008)] and during hydraulic fracturing experiments in the hydrocarbon industry [*Tary et al.*(2014)], due to the resonance of fluid-filled cavities.

7 Conclusions

We detected deep icequakes at Glacier d'Argentière at depths down to 130 m, which was shallower than the ice/bed interface. Most of the events were deeper than the maximum depth of open crevasses. Although such events have been detected in previous studies [*Deichmann et al.*(2000), *Walter et al.*(2008), *Walter et al.*(2009), *Röösli et al.*(2014)], this is the first time that so many events have been detected and located. These events are clustered in time and space. The distribution of the interevent times and the amplitudes can both be fitted by power laws, although with exponents that are larger than commonly observed for earthquakes [*Bak et al.*(2002)]. We suggest hydraulic fracturing as a potential source mechanism for these events for several reasons. First, the polarities of the P-waves for all of the events are consistent with tensile failure. Fractures cannot propagate within the ice below about 30 m, and they remain open unless they are filled with water

[*Van der Veen*(1998), *Van der Veen*(2007)]. Second, the largest burst of deep icequakes coincided with strong warming and rapid decrease in snow height, as well as with transient acceleration of glacier motion. These observations suggest that meltwater had infiltrated down to the ice/bed interface. Moreover, the presence of hybrid events and of a gliding harmonic tremor, which are analogous to volcanic tremor and to seismic resonance observed during industrial hydraulic-fracturing experiments, suggests the existence of water-filled cavities. Finally, the large exponent b of the amplitude distribution is reminiscent of that observed for earthquakes induced by geothermal activity and triggered by hydraulic fracturing [*Grünthal*(2013)].

A strong increase in the temperature occurred between 25 and 28 April and produced a decrease in the snow height of 60 cm, which was probably mainly due to snowmelting. Meltwater might have infiltrated into open fractures and promoted their propagation. These fractures were progressively filled with water and generated the resonant seismic noise and the hybrid signals. A large number of deep icequakes occurred on 28 April at greater depths than before 12 April. The acceleration of the glacier on 29 April further suggests that the meltwater had reached the ice/bed interface, although the clusters of deep icequakes detected do not reach the ice/bed interface. The harmonic tremor intensified on the evening of 28 April, and weakened in the following days. The resonance frequency showed several decreasing steps that were sometimes associated with bursts of deep icequakes. These steps might be due to crevasse propagation, which decreases the resonance frequency of water-filled cavities. The resonance frequency also showed a progressive increase between 32 Hz on 24 April and 38 Hz on 3 May. Fluctuations of the water level can modify the length of the resonating fluid-filled cavity, and can also explain variations of the resonance frequency. As several factors influence the resonance frequency (e.g., water level, fracture width and length), it is difficult to interpret our observations without additional measurements.

[*Walter et al.*(2013)] detected deep basal icequakes in Switzerland with the seismic moment tensor corresponding to either fracture opening or fracture collapse, with both event types occurring at the same location. In this study, we did not detect any deep icequakes with dilatational first motion ("down"), that would indicate fracture closing. We searched for crack-collapse events by reversing the polarity of the template signal for cluster B and looking for similar events in the full continuous seismic signal; however, no events were found. This suggests that in our study, while fracture opening produces seismic signals, fracture closing is due to creep and is aseismic.

Many deep icequakes occurred before 12 April, when the temperature was below freezing most of the time, and when no resonance was observed. These events were thus unlikely to have been triggered by hydraulic fracturing. These events were as deep as 60 m, which was deeper than the maximum depth of the open crevasses, given by the depth where the stress intensity factor is equal to the fracture toughness of the ice [*Van der Veen*(2007)]. Water-free fractures can propagate below that depth, but will then progressively close by creep, due to the ice overburden pressure.

This study focussed on the time period between 30 March and 3 May 2012, when most of the deep icequakes occurred. Several weeks of seismic data are also available for February and March 2012, although very few deep icequakes were detected during that time. No deep event was detected between June 5 and 19, although the meltwater production was much higher in June than in April. An interpretation here is that the water pressure was much higher early in the spring. The water pressure decreases in summer, when an efficient drainage system has developed [*Fountain and Walder*(1998)] and it might not be sufficient for hydraulic fracturing. To conclude, further studies are required with a larger number of seismic sensors, and a higher sampling rate, to better constrain the location of the deep englacial icequakes and their source mechanism.

Acknowledgments. We thank the Editor, the Associate Editor and two anonymous reviewers for carefully reading the manuscript and providing many constructive suggestions. We thank Fabian Walter, Francesca Raimondi, Olivier Michel, Claudia Röösli, Pierre Dalban, Christian Vincent, Daniel Amorese, Jean-Baptiste Tary and Michel Bouchon for useful discussions. The meteorological data were obtained from Météo-France and from the GLACIOCLIM database. GLACIOCLIM is supported by INSU and OSUG. We thank Laurent Ott, Olivier Michel and others for participating in the installation and maintenance of the seismic network. This work was supported by PEPS CNRS and by a grant from Labex OSUG@2020 (ANR10 LABX56). P. Comon is supported by the ERC AdG 2013-320594 DECODA. ISTerre and SigmaPhy team are part of Labex OSUG@2020 (ANR10 LABX56). The seismic data used in this study can be downloaded from `ftp://ftp.osug.fr:/pub/DATA_JGR_ARGENTIERE`.

References

[*Bak et al.*(2002)] Bak, P., K. Christensen, L. Danon, and T. Scanlon (2002), Unified scaling law for earthquakes, *Phys. Rev. Lett., 88*, 178501.

[*Bocquet and Ricq*(1977)] Bocquet, G., and J. C. Ricq (1977), Measurement of ice movement in subglacial cavities: a new cavitometer beneath the Glacier d'Argentière (Mt Blanc, France), *J. Glaciol., 18*(78), 137-142.

[*Carmichael et al.*(2012)] Carmichael, J. D., E. C. Pettit, M. Hoffman, A. Fountain, and B. Hallet (2012), Seismic multiplet response triggered by melt at Blood Falls, Taylor Glacier, Antarctica, *J. Geophys. Res., 117*, F03004, doi:10.1029/2011JF002221.

[*Chouet*(1986)] Chouet, B. (1986), Dynamics of a fluid-driven crack in three dimensions by the finite difference method, *J. Geophys. Res., 91*, 13,967-13,992.

[*Dalban Canassy et al.*(2013)] Dalban Canassy, P., F. Walter, S. Husen, H. Maurer, J. Faillettaz, and D. Farinotti (2013), Investigating dynamics of an Alpine glacier using probabilistic icequake locations (Triftgletscher, Switzerland), *J. Geophys. Res. Earth Surf., 118*, 2003-2018, doi:10.1002/jgrf.20097.

[*Deichmann et al.*(2000)] Deichmann, N., J. Ansorge, F. Scherbaum, A. Aschwanden, F. Bernhardi, and G. H. Gudmundsson (2000), Evidence for deep icequakes in an Alpine glacier, *Ann. Glaciol., 31*(1), 85-90.

[*Faillettaz et al.*(2011)] Faillettaz J, M. Funk, and D. Sornette (2011), Icequakes coupled with surface displacements for predicting glacier break-off, *J. Glaciol., 57*(203), 453-460, doi:10.3189/002214311796905668.

[*Fountain and Walder*(1998)] Fountain, A. G., and J. S. Walder (1998), Water flow through temperate glaciers, *Rev. Geophys. 36*, 299-328.

[*Fountain et al.*(2005)] Fountain, A. G., R. W. Jacobel, R. Schlichting, and P. Jansson (2005), Fractures as the main pathways of water flow in temperate glaciers, *Nature, 433*(7026), 618-621.

[*Grünthal*(2013)] Grünthal, G. (2014), Induced seismicity related to geothermal projects versus natural tectonic earthquakes and other types of induced seismic events in Central Europe. *Geothermics, 52*, 22-35.

[*Heeszel et al.*(2014)] Heeszel, D. S., F. Walter, and D. L. Kilb (2014), Humming glaciers, *Geology, 42*(12), 1099-1102, doi:10.1130/G35994.1.

[*Helmstetter et al.*(2005)] Helmstetter, A., Y. Y. Kagan, and D. D. Jackson (2005), Importance of small earthquakes for stress transfers and earthquake triggering, *J. Geophys. Res., 110*, B05S08, doi:10.1029/2004JB003286.

[*Helmstetter and Garambois*(2010)] Helmstetter, A., and S. Garambois (2010), Seismic monitoring of Séchilienne Rockslide (French Alps) : analysis of seismic signals and their correlation with rainfalls, *J. Geophys. Res., 115*, F03016, doi:10.1029/2009JF001532.

[*Helmstetter et al.*(2014)] Helmstetter, A., B. Nicolas, P. Comon, and M. Gay (2014), Basal icequakes recorded beneath an alpine glacier (Glacier d'Argentière, Mont Blanc, France) : evidence for stick-slip motion? *in press in J. Geophys. Res.*, doi:10.1002/2014JF003288.

[*Konstantinou and Schlindwein*(2008)] Konstantinou, K. I., and V. Schlindwein (2003), Nature, wavefield properties and source mechanism of volcanic tremor: A review. *J. Volcanol. Geoth. Res., 119*, 161-187.

[*Korneev*(2008)] Korneev, V. (2008), Slow waves in fractures filled with viscous fluid, *Geophysics, 73*, N1-N7, doi:10.1190/1.2802174.

[*Métaxian, et al.*(2003)] Métaxian, J.-P., S. Araujo, M. Mora, and P. Lesage (2003), Seismicity related to the glacier of Cotopaxi Volcano, Ecuador, *Geophys. Res. Lett., 30*(9), 1483, doi:10.1029/2002GL016773.

[*Michelini and Bolt*(1986)] Michelini, A., and B. A. Bolt (1986), Application of the principal parameters method to the 1983 Coalinga, California, aftershock sequence, *Bull. Seismol. Soc. Am., 76*(2), 409-420.

[*Mikesell, et al.*(2012)] Mikesell, T. D., K. van Wijk, M. M. Haney, J. H. Bradford, H. P. Marshall, and J. T. Harper (2012), Monitoring glacier surface seismicity in time and space using Rayleigh waves, *J. Geophys. Res., 117*, F02020, doi:10.1029/2011JF002259.

[*Moreau*(1999)] Moreau, L. (1999), Synthèse des variations de l'hydrographie sous-glaciaire du glacier d'Argentière de 1970 à 1999, *La Houille blanche, 99*(5), 40-46.

[*Neave and Savage*(1970)] Neave, K. G., and J. C. Savage (1970), Icequakes on the Athabasca Glacier, *J. Geophys. Res., 75*(8), 1351-1362.

[*Nelder and Mead*(1965)] Nelder, J. A., and R. Mead (1965), A simplex method for function minimization, *Computer Journal, 7*, 308313. doi:10.1093/comjnl/7.4.308.

[*Neuberg and Pointer*(2000)] Neuberg, J., and T. Pointer (2000), Effects of volcano topography on seismic broad-band waveforms, *Geophys. J. Int., 143*, 239-248.

[*O'Neel et al.*(2007)] O'Neel, S., H. Marshall, D. McNamara, and W. Pfeffer (2007), Seismic detection and analysis of icequakes at Columbia Glacier, Alaska, *J. Geophys. Res., 112*, F03S23, doi:10.1029/2006JF000595.

[*Paterson*(1994)] Paterson, W. (1994), *The Physics of Glaciers*, 3rd ed., Pergamon, New York.

[*Röösli et al.*(2014)] Röösli, C., F. Walter, S. Husen, L. Andrews, M. P. Lüthi, G. A. Catania, and E. Kissling (2014), Sustained seismic tremors and icequakes detected in the ablation zone of the Greenland ice sheet, *J. Glaciol., 60*(221), 563-575, doi:10.3189/2014JoG13J210.

[*Roux et al.*(2008)] Roux, P., D. Marsan, J., Métaxian, G., O'Brien, and L. Moreau (2008), Microseismic activity within a sérac zone in an Alpine glacier (glacier d'Argentière, Mont Blanc, France), *J. Glaciol., 54*(184), 157-168.

[*Schorlemmer et al.*(1997)] Schorlemmer, D., S. Wiemer, and M. Wyss (2005), Variations in earthquake-size distribution across different stress regimes, *Nature, 437*(7058), 539-542.

[*St. Lawrence and Qamar*(1979)] St. Lawrence, W. S., and A. Qamar (1979), Hydraulic transients: A seismic source in volcanoes and glaciers, *Science, 203*(4381), 654-656.

[*Tary et al.*(2014)] Tary, J., M. Baan, and D. Eaton (2014), Interpretation of resonance frequencies recorded during hydraulic fracturing treatments, *J. Geophys. Res., 119*, 1295-1315, doi:10.1002/2013JB010904.

[*Vallon*(1967)] Vallon, M. (1967), *Contribution à l'étude de la Mer de Glace*, Ph.D. thesis, Univ. of Grenoble, France.

[*Vallon*(1981)] Vallon, M. (1981), Pétrographie de la glace du glacier d'Argentière, Proceedings of the Annual meeting of the Société Hydrotechnique de France Section Glaciologie, 7p.

[*Van der Veen*(1998)] Van der Veen, C. J. (1998), Fracture mechanics approach to penetration of surface crevasses on glaciers, *Cold Reg. Sci. Tech. 27*(1), 31-47.

[*Van der Veen*(1998)] Van der Veen, C. J. (1998), Fracture mechanics approach to penetration of bottom crevasses on glaciers, *Cold Reg. Sci. Tech. 27*(3), 213-223.

[*Van der Veen*(2007)] Van der Veen, C. J. (2007), Fracture propagation as means of rapidly transferring surface meltwater to the base of glaciers, *J. Geophys. Res., 34*, doi:10.1029/2006GL028385.

[*Vidale*(1986)] Vidale, J. (1986), Complex polarization analysis of particle motion, *Bull. Seismol. Soc. Am., 76*(5), 1393-1405.

[*Vincent et al.*(2009)] Vincent, C., A. Soruco, D. Six, and E. Le Meur (2009), Glacier thickening and decay analysis from 50 years of glaciological observations performed on Glacier d'Argentière, Mont Blanc area, France, *Ann. Glaciol., 50*, 73-79.

[*Vivian and Bocquet*(1973)] Vivian, R., and G. Bocquet (1973), Subglacial cavitation phenomena under the glacier d'Argentière, Mont Blanc, France, *J. Glaciol., 12*(66), 439-451.

[*Walter et al.*(2008)] Walter, F., Deichmann, N., and Funk, M. (2008), Basal icequakes during changing subglacial water pressures beneath Gornergletscher, Switzerland. *J. Glaciol., 54*(186), 511-521.

[*Walter et al.*(2009)] Walter, F., J. Clinton, N. Deichmann, D. Dreger, S. Minson, and M. Funk (2009), Moment tensor inversion of icequakes on Gornergletscher, Switzerland, *Bull. Seismol. Soc. Am., 99*(2A), 852-870.

[*Walter et al.*(2010)] Walter, F., D. Dreger, J. Clinton, N. Deichmann, and M. Funk (2010), Evidence for near-horizontal tensile faulting at the base of Gornergletscher, a swiss Alpine glacier, *Bull. Seismol. Soc. Am., 100*(2), 458-472, doi:10.1785/0120090083.

[*Walter et al.*(2013)] Walter, F., P. Dalban Canassy, S. Husen, and J. F. Clinton (2013), Deep icequakes: What happens at the base of Alpine glaciers?, *J. Geophys. Res. Earth Surf., 118*, 1720-1728, doi:10.1002/jgrf.20124.

[*Weiss*(1997)] Weiss, J. (1997), The role of attenuation on acoustic emission amplitude distributions and *b*-values, *Bull. Seismol. Soc. Am., 87*(5), 1362-1367.

[*West et al.*(2010)] West, M. E., C. F. Larsen, M. Truffer, S. ONeel, and L. LeBlanc (2010), Glacier microseismicity, *Geology, 38*(4), 319-322.

[*Winberry et al.*(2009)] Winberry, J. P., S. Anandakrishnan, and R. B. Alley (2009), Seismic observations of transient subglacial water-flow beneath MacAyeal Ice Stream, West Antarctica, *Geophys. Res. Lett., 36*, L11502, doi:10.1029/2009GL037730.

[*Winberry et al.*(2013)] Winberry, J. P., S. Anandakrishnan, D. A. Wiens, and R. B. Alley (2013), Nucleation and seismic tremor associated with the glacial earthquakes of Whillans Ice Stream, Antarctica, *Geophys. Res. Lett., 40*, 312-315, doi:10.1002/grl.50130.

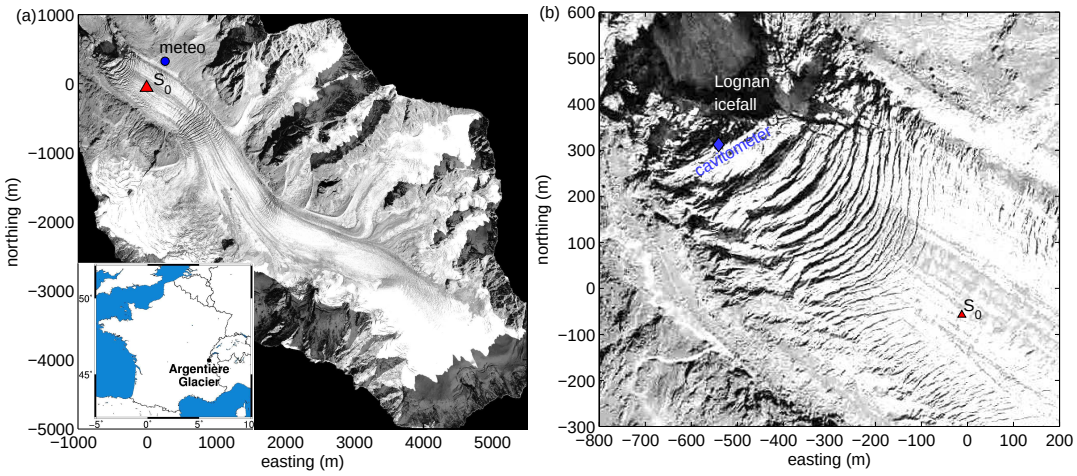

Figure 1: (a) Orthophotograph of the glacier taken in 2003 (from GLACIOCIM) (a) and (b) zoom around the seismometer. The seismometer is shown by a triangle and the GLACIOCLIM meteorological station by a circle. The blue diamond in (b) marks the location of the cavitometer in a subglacial cavity. The grid origin is 45.964 degrees N and 6.973 degrees E.

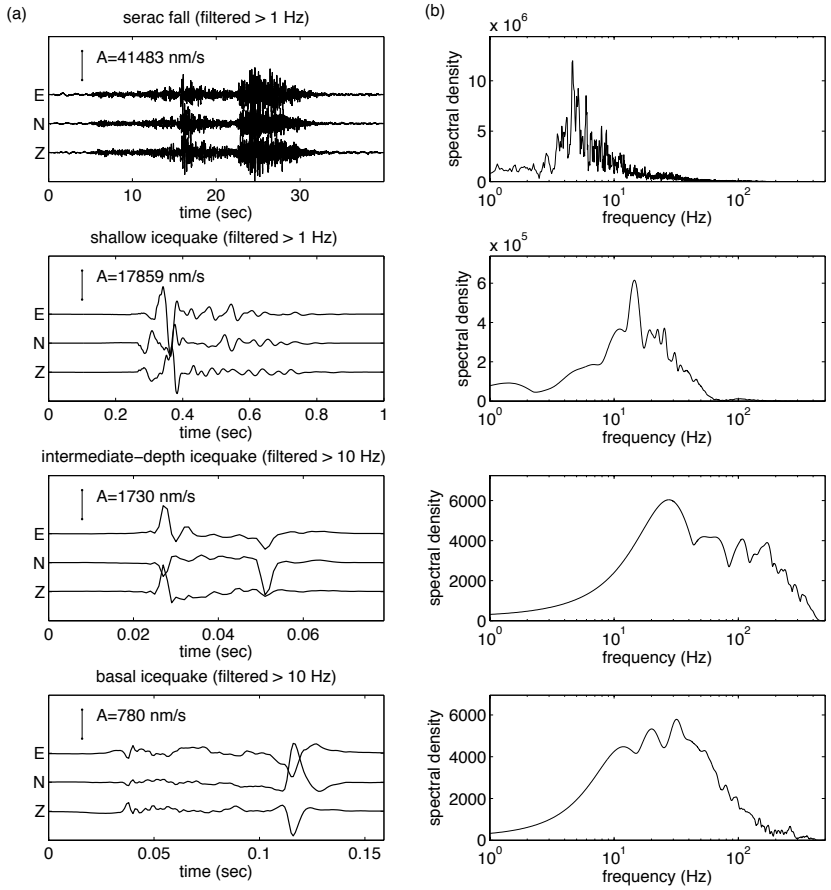

Figure 2: (a) Waveforms and (b) Fourier transform for the different types of events. The signals were converted to ground velocity and high-pass filtered. Note the different time scales for the waveforms.

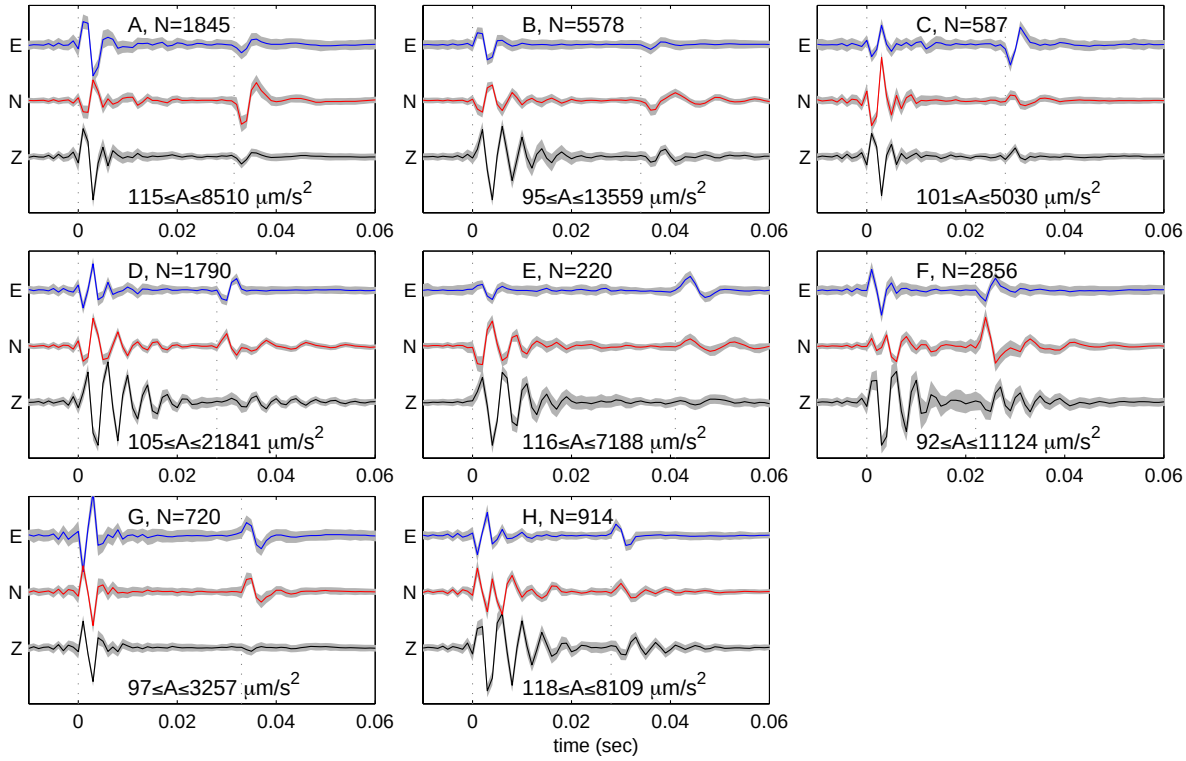

Figure 3: Waveforms of template events for all of the clusters. Dotted lines indicate the arrival times of the P-waves and S-waves. Gray patches show the variability of the signal for all of the events of each cluster (one standard deviation of signals aligned on the P-waves and S-waves, and normalized according to the peak amplitude). The number of events in each cluster and the range of peak acceleration A are indicated in each plot.

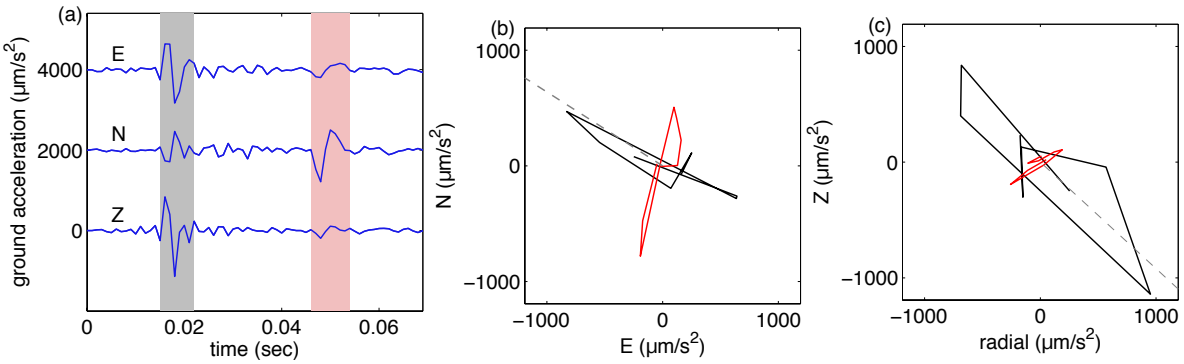

Figure 4: (a) Waveforms of a basal icequake of type A. The shaded areas indicate the time intervals of the P-waves and S-waves. The polarization method of [*Vidale*(1986)] provides an estimate of the azimuth $\alpha = 303$ degrees N and of the apparent angle of incidence $\phi = 47$ degrees of the P-waves. (b) Particle motion for the P-waves (black) and S-waves (red) in the horizontal plane for the time intervals highlighted in (a). (c) Particle motion in the vertical plane parallel to the direction α. Dashed lines show the azimuth direction in (b) and the apparent incidence angle in (c) for the P-waves.

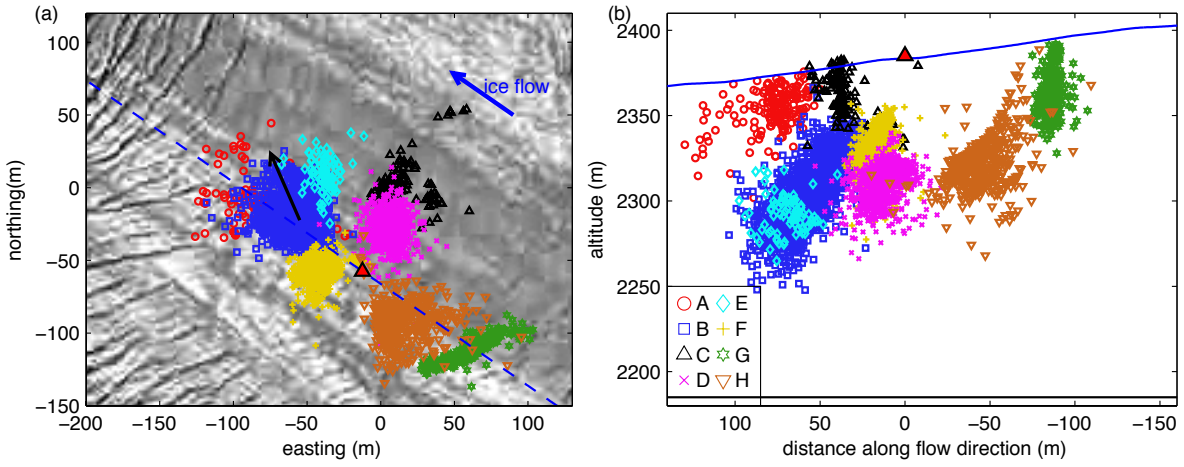

Figure 5: (a) Map of the icequakes for all of the events with peak amplitude $A > 300\ \mu m/s^2$, $\phi < \phi^*$ and correlation $C \geq 0.7$. For cluster B, the black arrow shows the dip direction. (b) Cross-section in the glacier flow direction. The blue line shows the ice surface along the dashed blue line shown in (a), and the black line indicates the ice/rock interface. The seismic sensor is shown by a red triangle.

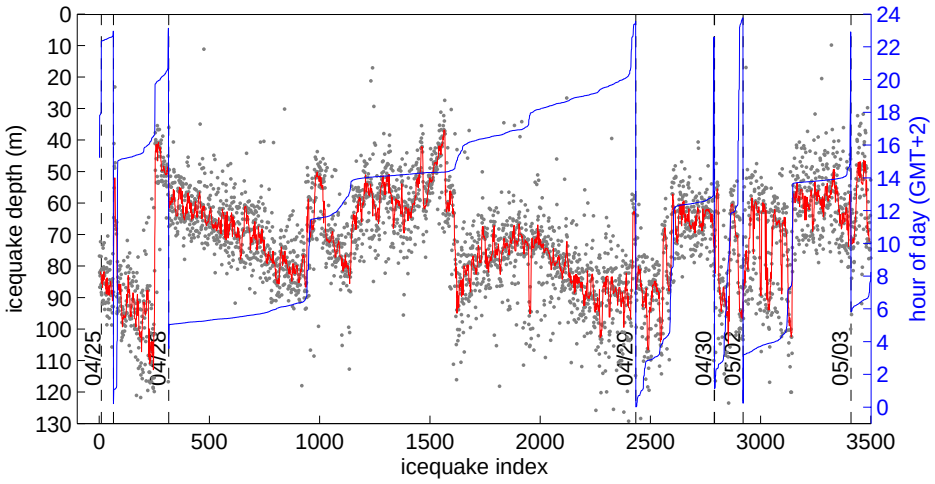

Figure 6: Icequakes depths (dots) and median values for a sliding window of 10 events (red), for all icequakes of cluster B with peak amplitude $A > 300\ \mu m/s^2$ and correlation $C \geq 0.7$. The blue line indicates the hour of the day (local time), and each vertical dashed line indicates a new day.

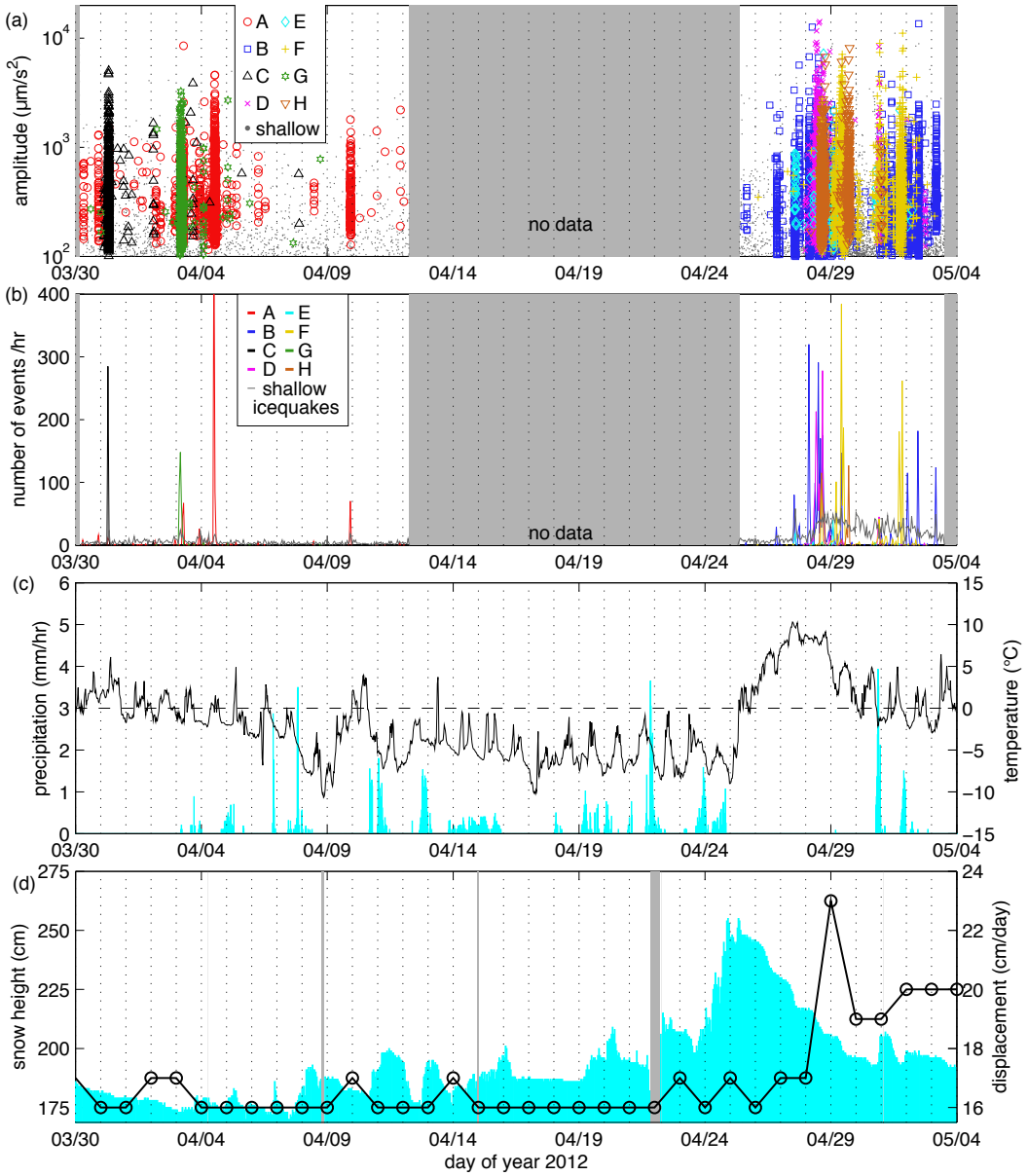

Figure 7: (a) Time series of the signal peak amplitudes for each cluster. (b) Number of shallow and deep events per hour with peak amplitude $A > 300\ \mu m/s^2$. Note that the largest peak on 4 April is not to scale (507 events per hour). (c) Hourly precipitation (from the Le Tour Météo-France station) and temperature (from the GLACIOCLIM database). (d) Snow height (from Aiguilles Rouges Météo-France station) and daily basal displacement measured by the cavitometer beneath Lognan ice fall. Gray shaded areas (a,b), when no data were available.

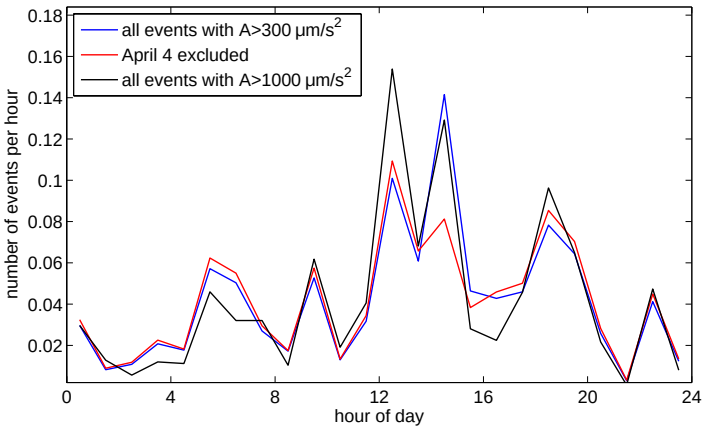

Figure 8: Diurnal distribution of the icequakes for different amplitude thresholds: $A > 300\ \mu m/s^2$ (blue, red) or $A > 1000\ \mu m/s^2$ (black). Times are local (Greenwich Mean Time +2 h). The strong peak at 14:00 disappears when events that occurred on 4 April were excluded (red).

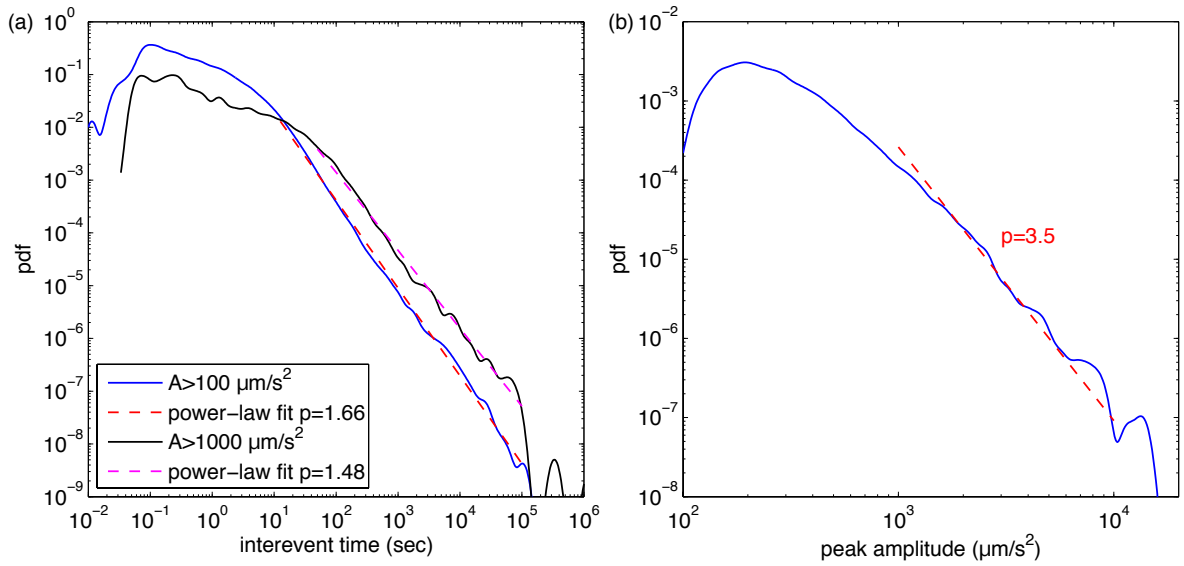

Figure 9: (a) Probability density function of the interevent times for different amplitude thresholds. (b) Probability density function of the peak amplitudes. Dashed lines show the power-law fits.

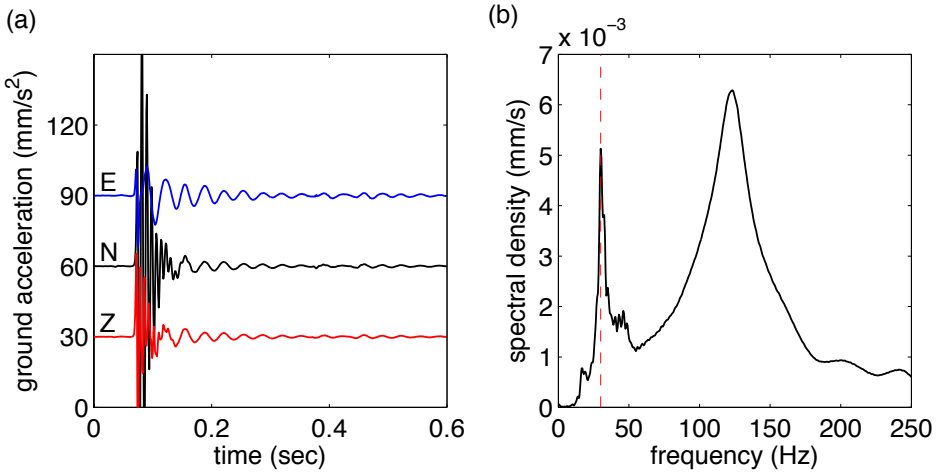

Figure 10: (a) Seismograms and (b) spectral density for a hybrid icequake that occurred on 29 April at 21:49 UTC, with a high-frequency onset followed by a monochromatic coda with a frequency of 30 Hz (dashed line).

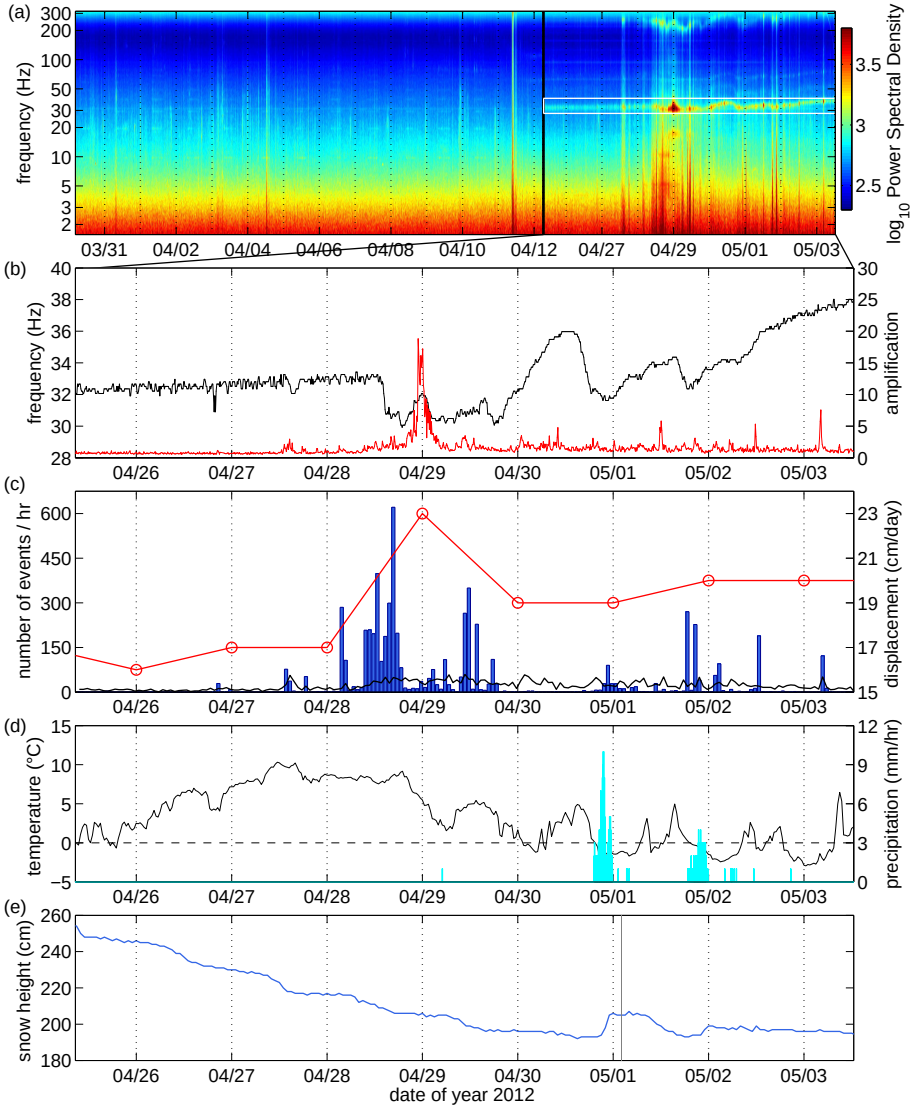

Figure 11: (a) Spectrogram of seismic noise (in a logarithmic color-scale). The thick vertical line indicates a gap in the monitoring between 12 and 25 April, 2012. The white rectangle indicates the time and frequency interval considered in (b). (b) Temporal variation of the resonance frequency f_r and amplification factor (amplitude of the normalized spectra for $f = f_r$) after the gap. (c) Hourly rate of shallow (solid line) and deep (histogram) icequakes. Circles show daily basal motion. (d) Temperature (from GLACIOCLIM database) and hourly precipitation (from Le Tour Météo-France station). (e) Snow height at Aiguilles Rouges Météo-France station.